Transition from ferromagnetic to noncollinear to paramagnetic state with increasing Ru concentration in FeRu films

Juliana Lisik [1,*,†] Manuel Rojas [1,*,‡] Spencer Myrtle,[1] Dominic H. Ryan [2,§] René Hübner [3] Pavlo Omelchenko [1]
Claas Abert [4] Amil Ducevic [4] Dieter Suess [4] Ivan Soldatov [5] Rudolf Schaefer [5] Johannes Seyd [6]
Manfred Albrecht [6] and Erol Girt [1,¶]

[1]*Department of Physics, Simon Fraser University, 8888 University Drive, Burnaby, British Columbia, Canada V5A 1S6*
[2]*Physics Department and Centre for the Physics of Materials, McGill University, 3600 University Street, Montreal, Quebec, Canada H3A 2T8*
[3]*Institute of Ion Beam Physics and Materials Research, Helmholtz-Zentrum Dresden-Rossendorf,*
Bautzner Landstraße 400, 01328 Dresden, Germany
[4]*Physics of Functional Materials, Faculty of Physics, University of Vienna, Kolingasse 14–16, 1090 Vienna, Austria*
[5]*Leibniz Institute for Solid State and Materials Research Dresden, Helmholtzstraße 20, 01069 Dresden, Germany*
[6]*Institute of Physics, University of Augsburg, Universitätsstraße 1, 86159 Augsburg, Germany*

The structural and magnetic properties of sputter-deposited $Fe_{100-x}Ru_x$ films were studied for $x \leqslant 50$. The crystal structure of $Fe_{100-x}Ru_x$ is shown to be predominantly body-centered cubic for $x < 13$ and to undergo a gradual transition to hexagonal close-packed in the Ru concentration range $13 \lesssim x \lesssim 20$. Magnetic measurements indicate that the addition of Ru to Fe gives rise to a noncollinear magnetic alignment between Fe atoms in the body-centered cubic FeRu alloys, while the hexagonal close-packed FeRu alloys exhibit paramagnetic behavior. A simple atomistic model was used to show that the competition between ferromagnetic coupling of neighboring Fe atoms and antiferromagnetic coupling of Fe atoms across Ru atoms in cubic FeRu structures can induce noncollinear magnetic order. Magnetic multilayer structures used in thin-film magnetic devices make extensive use of both Fe and Ru layers. Our results reveal that the presence of even a small amount of Ru in Fe influences the magnetic order of Fe, which could impact the performance of these devices.

I. INTRODUCTION

Iron is the most abundant element in the Earth by mass, composing about 80 % of Earth's core; furthermore, it is the fourth most abundant element in Earth's crust [1]. The structural, electrical, and magnetic properties of iron and its alloys are at the root of many applications. Of the three elements that have ferromagnetic alignment above room temperature (iron, cobalt, and nickel), iron has the largest saturation magnetization, making iron alloys a crucial component of magnetic devices (e.g., hard and soft magnets, magnetic sensors, and recording media). However, despite centuries of research, understanding the phase diagram and magnetic properties of iron alloys remains an active research topic.

The unary phase diagram of Fe consists of three crystal structures that meet at a triple point located at approximately $477\,°C$ and $11\,GPa$. At standard temperature and pressure, Fe is body-centered cubic (bcc), known as α-Fe, and has well-known ferromagnetic order. The crystal structure transitions from bcc to face-centered cubic (fcc) at high temperatures. At

pressures above $11\,GPa$, the crystal structure of Fe transitions from bcc to hexagonal close-packed (hcp), known as ϵ-Fe. The hcp Fe phase is stable for pressures and temperatures corresponding to the conditions of Earth's core [2]. At the transition from bcc to hcp Fe, there is a rapid decrease in magnetic moment [3]. However, unlike bcc Fe, the magnetic state of hcp Fe is not well understood. Some experimental studies find that hcp Fe does not appear to have any long-range magnetic order, as determined from low-temperature Mössbauer measurements [4,5], x-ray magnetic circular dichroism [3], and neutron powder diffraction [6]. X-ray emission spectroscopy, on the other hand, detects a localized magnetic moment for hcp Fe between about 12 and $40\,GPa$ [6,7] with a magnitude of $0.74\,\mu_B$ at $20\,GPa$ [6]. More recently, a ground state of alternating antiferromagnetic and nonmagnetic atomic layers was used to explain the conflicting experimental observations discussed above [6].

Thin-film magnetic devices make extensive use of not only Fe but also Ru layers [8–10]. Thus, it is important to study how the presence of Ru in Fe, which can occur during deposition or annealing, affects the magnetic properties of Fe. When Fe is alloyed with Ru, not only the bcc phase but also the hcp phase can be stabilized at standard temperature and pressure. The bcc phase of FeRu has been seen for up to 4 at. % of Ru in Fe [11]. Recent studies suggest that this phase of FeRu is ferromagnetic [12], as is pure Fe. Additionally, Mössbauer studies of bulk bcc FeRu argue for the presence of spin and

---
*These authors contributed equally to this work.
†Contact author: jbesler@sfu.ca
‡Contact author: mrojas@sfu.ca
§Contact author: dhryan@physics.mcgill.ca
¶Contact author: egirt@sfu.ca

104429-1

charge density waves in the vicinity of the Ru impurities in Fe [13]. As more Ru is added, the hcp phase appears: it has been seen above 23 at. % of Ru in the equilibrium phase diagram [11]. There are many parallels between hcp FeRu and high-pressure hcp Fe; however, theoretical and experimental studies of FeRu are scarce. Similar to high-pressure Fe studies, during the transition from bcc to hcp, the magnetization of FeRu collapses. The magnetic structure of the hcp FeRu alloy remains a debated topic. Early Mössbauer studies did not observe any hyperfine structure, but the existence of an antiferromagnetic phase with a magnetic moment of about $0.1\mu_B$ was estimated [14,15]. More recent Mössbauer studies suggest that hcp FeRu is paramagnetic [12], but neutron diffraction studies of bulk hcp $Fe_{71}Ru_{29}$ reported an incommensurate antiferromagnetic state with a Néel temperature of 124 K and a low-temperature Fe magnetic moment of about μ_B [16]. Theoretical work on the ground state of $Fe_{50}Ru_{50}$ identifies a type-II antiferromagnetic phase as the lowest energy state [17].

More recently, thin-film FeRu has been shown to mediate a large noncollinear magnetic coupling between two ferromagnetic layers [18]. The coupling angle and strength was controlled by the concentration of Ru within the FeRu alloy. Controlling the coupling angle is important for the design of magnetic thin-film devices, as the optimal structure almost always requires noncollinear alignment between at least two adjacent ferromagnetic films [19–22]. At present, it is not clear what role the bcc and hcp structures within the FeRu alloy play in the observed noncollinear coupling.

In this paper, we investigate the structural and magnetic properties of FeRu films over a composition range from 0 to 50 at. % of Ru in Fe. The emphasis is on the Ru concentration range from 0 to 20 at. %, within which the transition from bcc to hcp crystal structure occurs. Structural properties are explored with x-ray diffraction (XRD) and transmission electron microscopy (TEM), and magnetic properties are explored with Mössbauer spectroscopy, vibrating sample magnetometry (VSM), magneto-optical Kerr effect (MOKE) microscopy, and Lorentz transmission electron microscopy (LTEM). Our results show that, as Ru is added to ferromagnetic Fe films, the magnetic behavior of the films transitions to noncollinear and then to paramagnetic. Furthermore, we argue that the noncollinear order is a result of the competition between ferromagnetic coupling of neighboring Fe atoms and antiferromagnetic coupling of Fe atoms separated by Ru atoms.

II. EXPERIMENTAL DETAILS

Our studied films have the structure Ta(3.5)|Ru(3.5)| $Fe_{100-x}Ru_x(d)$|Ru(3.5), where the the numbers in parentheses indicate the layer thicknesses in nm, x is the atomic concentration of Ru in $Fe_{100-x}Ru_x$, and $d = 20$ or 100 nm is the thickness of the FeRu layer. The Ta seed layer is deposited to induce the $\langle 0001 \rangle$ growth orientation of the bottom Ru layer, and the top Ru layer protects the FeRu layer from oxidation. Throughout this paper, we will refer to Ta(3.5)|Ru(3.5)|$Fe_{100-x}Ru_x(d)$|Ru(3.5) films as Ta|Ru|$Fe_{100-x}Ru_x(d)$|Ru, as the thicknesses of the seed and capping layers were kept the same for all samples.

The studied films were deposited at room temperature with radio-frequency magnetron sputtering at an argon pressure below 2 mTorr. The base pressure of the system was below 5×10^{-8} Torr. (100) Si substrates were used for all studies except for Mössbauer spectroscopy, which required Kapton substrates to maximize the signal, and Lorentz transmission electron microscopy (LTEM), which used Si_3N_4 membranes. Selected films were annealed at 400 °C for 1 h to study the thermal stability of the crystal structure. For further sample preparation and deposition details, see Supplemental Material I [23]. Supplemental Material II [23] is a comparison of films grown on Si and Kapton substrates, confirming that the crystal structure and magnetic properties are not impacted by the choice of substrate.

Structural characterization of the deposited layers was carried out by x-ray diffraction (XRD) using CuK_α radiation. Out-of-plane θ-2θ, in-plane θ-2θ, and rocking curve measurements were performed. For the out-of-plane and in-plane θ-2θ measurements, the angle between the incident x-ray beam and the film surface, θ_1, is the same as the angle between the reflected x-ray beam and the film surface, θ_2, i.e., $\theta_1 = \theta_2 = \theta$. For the rocking curve measurement, $\theta_1 + \theta_2$ is kept constant and the sample is rocked by angle ω so that θ_1 varies from $\theta - \omega/2$ to $\theta + \omega/2$. The scattering wave vector is perpendicular to the film surface for the out-of-plane θ-2θ measurement and varies around the perpendicular direction for the rocking curve measurement. For the in-plane θ-2θ measurement, however, the scattering wave vector is almost parallel to the film surface, at an angle of $0.5°$.

To further characterize the film microstructure, bright-field and high-resolution transmission electron microscopy (HRTEM) imaging were performed on Ta|Ru|$Fe_{100-x}Ru_x(20)$|Ru ($x = 13$ and 17) and Ta|Ru|Fe(100)|Ru films on an FEI image-C_s-corrected Titan 80–300 microscope operated at an accelerating voltage of 300 kV. Scanning transmission electron microscopy (STEM) coupled with spectrum imaging analysis based on energy-dispersive x-ray spectroscopy (EDXS) was performed at 200 kV with an FEI Talos F200X microscope equipped with a Super-X EDX detector system. The HRTEM images were further examined by fast Fourier transform (FFT) analysis to detect the spatial distribution of different lattice structures. Prior to transmission electron microscopy analysis, the specimen, mounted in a high-visibility low-background holder, was placed into a Fischione Model 1020 Plasma Cleaner for 10 s to remove possible organic contamination.

The ^{57}Fe Mössbauer spectroscopy measurements were carried out on Ta|Ru|$Fe_{100-x}Ru_x(100)$|Ru ($0 \leqslant x \leqslant 50$), Ta|Fe(100)|Ta, and Fe(100) films. For each film, one deposition was performed, sputtering on Kapton film for Mössbauer measurements and on a 1 in. square Si substrate for magnetometry measurements. The Kapton film and the Si substrate were both taped to an 8-in.-diameter Si substrate for deposition. For conversion electron Mössbauer spectroscopy (CEMS) measurements, ~50-mm-diameter Kapton film samples were used, and for transmission Mössbauer spectroscopy (TMS) measurements, stacks of fifteen 15-mm square Kapton film samples were made. This is because TMS measurements require thicker samples to obtain a useful signal-to-noise ratio.
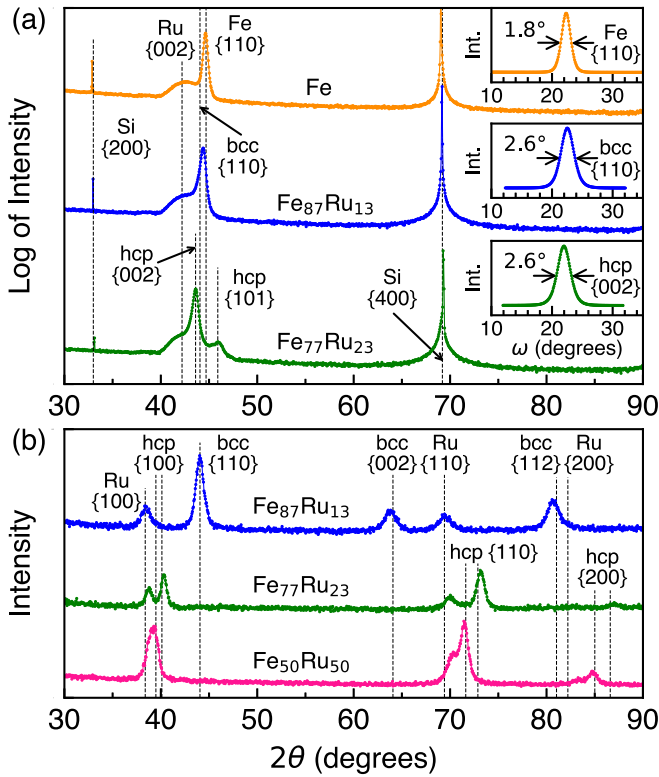
FIG. 1. (a) Out-of-plane and (b) in-plane θ-2θ measurements of as-deposited Ta(3.5)|Ru(3.5)|Fe$_{100-x}$Ru$_x$(100)|Ru(3.5) for $x = 0$, 13, 23, and 50. The inset plots in (a) represent the rocking curve measurements of the Fe {110}, bcc {110}, and hcp {002} reflections and include the full width at half maximum. Dashed lines are placed at the expected positions of diffraction peaks. Those labeled Fe and Ru correspond to bcc Fe and hcp Ru, respectively, and those labeled bcc and hcp correspond to bcc Fe$_{87}$Ru$_{13}$ and hcp Fe$_{100-x}$Ru$_x$ ($x = 23$ or 50), respectively. The Si {200} and {400} diffraction peaks in (a) are from the Si substrate.

Mössbauer measurements were performed using a 1.8 GBq ^{57}CoRh source driven in constant acceleration mode and calibrated using a thin bcc Fe foil. Isomer shifts are quoted relative to the centroid of the bcc Fe spectrum. Room-temperature CEMS measurements were collected using a conventional homemade detector. The ∼50-mm-diameter Kapton film sample is mounted inside the detector with a flowing 90% He + 10% CH$_4$ gas mixture used to detect the backscattered electrons. All films were measured at room temperature, but the Ta|Ru|Fe$_{100-x}$Ru$_x$(100)|Ru ($x = 18.5$ and 19.5) films were also measured with TMS at 9.7 and 9.9 K, respectively. Low temperatures were obtained by mounting the stacked samples in a vibration-isolated closed-cycle helium refrigerator. All films were measured at zero external magnetic field, but Fe(100) and Ta|Ru|Fe$_{100-x}$Ru$_x$(100)|Ru ($x = 0$, 4, and 8) were also measured in a 0.166 T magnetic field created by permanent magnets to remove magnetic domains. The magnetic components of the spectra were fitted using an assumed Gaussian distribution of hyperfine fields with independent widths to the high and low sides of the peak of the distribution. This form is needed to fit the clearly asymmetric magnetic patterns observed. The paramagnetic

components were fitted variously as symmetric doublets with a small, unresolved, quadrupole splitting; a Gaussian distribution of quadrupole splittings; and, where the two lines in the doublet are clearly of unequal intensity, two independent lines.

The field dependence of the magnetization, $M(H)$, of Ta|Ru|Fe$_{100-x}$Ru$_x(d)$|Ru ($d = 20$ and 100 nm), Ta|Fe(100)|Ta, and Fe(100) films was measured using a vibrating sample magnetometer and superconducting quantum interference device (SQUID) VSM in magnetic fields of up to 7 T and at temperatures of 295 and 5 K. Measurements were performed with the magnetic field applied parallel as well as perpendicular to the film surface.

A wide-field magneto-optical Kerr microscope was used to image magnetic domain structure in the Ta|Ru|Fe$_{96}$Ru$_4$(100)|Ru film. An external magnetic field was applied parallel to the film plane and the magnetic domain structure was observed, utilizing the longitudinal magneto-optical Kerr effect (MOKE) with two complementary sensitivity directions: along and transverse to the applied field.

The magnetic domain morphology of Ta|Ru|Fe$_{92}$Ru$_8$(20)|Ru was imaged by Lorentz transmission electron microscopy, at room temperature using a JEOL NEOARM-200F system operated at 200 keV beam energy in the Fresnel mode with an underfocus of −1 mm. Magnetic fields up to 2 T were applied along the electron beam direction, which is typically perpendicular to the film plane. To apply an in-plane magnetic field in addition to the out-of-plane magnetic field, the sample must be tilted by a tilt angle θ with respect to the film normal. The sample for LTEM was prepared by magnetron sputter deposition on a 30-nm-thick Si$_3$N$_4$ membrane, and images were acquired with a Gatan OneView camera.

III. FILM MICROSTRUCTURE

A. X-ray diffraction

XRD measurements were performed on Ta|Ru|Fe$_{100-x}$Ru$_x(d)$|Ru films for $d = 20$ and 100 nm. The out-of-plane and in-plane θ-2θ measurements of as-deposited Ta|Ru|Fe$_{100-x}$Ru$_x$(100)|Ru for $x = 0$, 13, 23, and 50 in Fig. 1 reveal that the Ru layers have hcp lattice structure, while the lattice structure of Fe$_{100-x}$Ru$_x$ depends on the Ru concentration, x. For $x = 23$ and 50, Fe$_{100-x}$Ru$_x$ has hcp lattice structure, and for $x = 13$, Fe$_{100-x}$Ru$_x$ has bcc lattice structure with no hcp lattice structure visible at the precision of our XRD measurements. We obtained this information by comparing the positions of the measured diffraction peaks with the expected positions of hcp and bcc diffraction peaks (represented by the dashed lines in Fig. 1) from previous XRD data as well as our own. Previous XRD data on hcp Ru and Fe$_{50}$Ru$_{50}$ [24] were used to determine the positions of the hcp Ru lines, the hcp Fe$_{50}$Ru$_{50}$ lines [in Fig. 1(b) only], and the hcp Fe$_{77}$Ru$_{23}$ lines (by extrapolation). Our out-of-plane and in-plane XRD data on bcc Fe and Fe$_{96}$Ru$_4$ (Fig. 3), which will be discussed later, were used to determine the positions of the bcc Fe line [in Fig. 1(a) only] and the bcc Fe$_{87}$Ru$_{13}$ lines (by extrapolation).

From the out-of-plane θ-2θ measurements in Fig. 1(a) for $x = 0$, 13 and 23, it is apparent that hcp Ru and Fe$_{77}$Ru$_{23}$
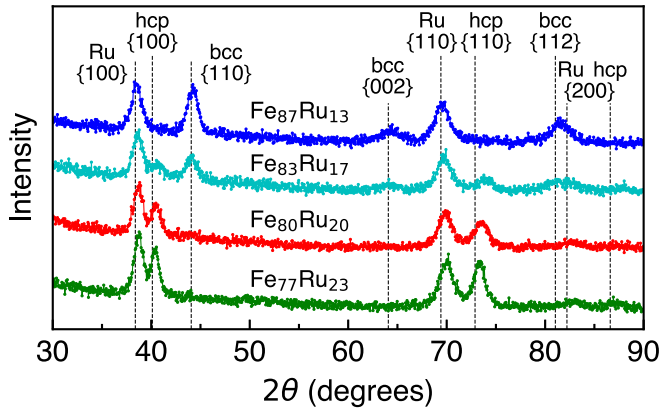
FIG. 2. In-plane θ-2θ measurements of as-deposited Ta(3.5)|Ru(3.5)|Fe$_{100-x}$Ru$_x$(20)|Ru(3.5) for x = 13, 17, 20, and 23. Dashed lines are placed at the expected positions of diffraction peaks. Those labeled Ru correspond to hcp Ru, and those labeled bcc and hcp correspond to bcc Fe$_{87}$Ru$_{13}$ and hcp Fe$_{77}$Ru$_{23}$, respectively.

have a {002} texture and that bcc Fe and Fe$_{87}$Ru$_{13}$ have a {110} texture. The diffraction pattern of hcp Fe$_{77}$Ru$_{23}$ also reveals a {101} diffraction peak with an intensity two orders of magnitude smaller than the {002} diffraction peak. The quality of the texture of the three films plotted in Fig. 1(a) is determined by rocking curve measurements, which are displayed in the inset plots above the spectrum of each film. The {110} reflection was measured for bcc Fe and Fe$_{87}$Ru$_{13}$, while the {002} reflection was measured for hcp Fe$_{77}$Ru$_{23}$. These plots indicate that the full width at half maximum (FWHM) of the rocking curve is 2.6° for the {110} reflection of Fe$_{87}$Ru$_{13}$ and the {002} reflection of Fe$_{77}$Ru$_{23}$, suggesting that our FeRu films are highly textured. For Fe, the FWHM of the rocking curve is 1.8° for the {110} reflection, indicating an even stronger texture. Figure 1(a) also shows Si {400} and a small trace of Si {200} reflections from the substrate. Si {200} is forbidden and could be a result of multiple diffraction of x rays in the crystal [25].

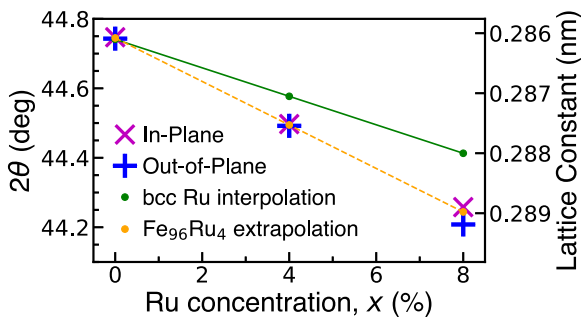FIG. 3. 2θ value of the bcc {110} diffraction peak from in-plane and out-of-plane θ-2θ XRD measurements of as-deposited Ta(3.5)|Ru(3.5)|Fe$_{100-x}$Ru$_x$(100)|Ru(3.5) (x = 0, 4, and 8). The corresponding lattice constants of the bcc structure are shown on the secondary axis. The bcc Ru interpolation is a linear function using the measured lattice constants of our Fe film and the lattice constant of a hypothetical bcc unit cell of Ru atoms with radius 0.1359 nm [30]. The Fe$_{96}$Ru$_4$ extrapolation is a linear function using the measured lattice constants of our Fe and Fe$_{96}$Ru$_4$ films. The size of the markers corresponds to the size of the error bars.

Our films are polycrystalline with grains textured along the growth direction and randomly oriented in the plane of the film. For this reason, out-of-plane θ-2θ measurements detect the planes along which the film is textured, while in-plane θ-2θ measurements can detect reflections from a range of planes perpendicular to the film surface. For the in-plane x-ray measurements, the diffraction pattern remains unaffected by the direction of the incident beam direction, owing to the random in-plane orientation of the grains. In contrast, if the sample has a single crystal structure, the incident beam must be precisely oriented with respect to the crystal lattice to obtain the diffraction pattern for in-plane measurements. Consequently, in-plane x-ray measurements allow one to distinguish between textured polycrystalline and single crystal samples. The in-plane θ-2θ measurements for x = 13, 23, and 50 are presented in Fig. 1(b). These measurements show that, for hcp Ru, hcp Fe$_{77}$Ru$_{23}$, and hcp Fe$_{50}$Ru$_{50}$, we observe reflections from the {100}, {110}, and {200} planes. For each of these families of planes, the expected diffraction peak positions for Ru, Fe$_{77}$Ru$_{23}$, and Fe$_{50}$Ru$_{50}$ are shown. For bcc Fe$_{87}$Ru$_{13}$, we observe reflections from the {110}, {002}, and {112} planes. Figure 1(b) shows that, as the concentration of Ru in Fe$_{100-x}$Ru$_x$ increases from 23 to 50 at.%, the {100}, {110}, and {200} hcp diffraction peaks shift to lower angles, indicating an increase in the lattice parameters of the FeRu layer. This is expected, because Fe and Ru form a solid solution in this composition range and Ru atoms are larger than Fe atoms. As the concentration of Ru is decreased from 23 to 13 at.%, Fig. 1(b) indicates that Fe$_{100-x}$Ru$_x$ transitions from hcp to bcc. These observations are consistent with previous structural FeRu studies [15,26,27].

In-plane θ-2θ XRD measurements of 20-nm-thick FeRu films, Ta|Ru|Fe$_{100-x}$Ru$_x$(20)|Ru, are presented in Fig. 2 for x = 13, 17, 20, and 23. The expected diffraction peak positions are calculated in the same way as those in Fig. 1 and are again represented by dashed lines. The expected positions for bcc Fe$_{100-x}$Ru$_x$ (x = 13 and 17) are very close together, as well as the positions for hcp Fe$_{100-x}$Ru$_x$ (x = 17, 20, and 23). Consequently, in Fig. 2, we only included the expected diffraction peak positions for bcc Fe$_{87}$Ru$_{13}$ and hcp Fe$_{77}$Ru$_{23}$. As expected, the lattice structure of the 20-nm-thick films (Fig. 2) is the same as that of the 100 nm-thick films [Fig. 1(b)]. For both thicknesses, only diffraction peaks corresponding to bcc lattice structure can be detected for Fe$_{87}$Ru$_{13}$, and only peaks corresponding to hcp lattice structure can be detected for Fe$_{77}$Ru$_{23}$. For the first intermediate composition in Fig. 2, Fe$_{83}$Ru$_{17}$, both bcc and hcp reflections are visible, but for Fe$_{80}$Ru$_{20}$, only hcp reflections are clearly visible.

We also explored the structural properties of Ta|Ru|Fe$_{100-x}$Ru$_x$(20)|Ru (x = 13 and 20) after annealing at 400°C, the typical annealing temperature of the CMOS fabrication process [28,29], for 1 h. The Ru concentration x = 13 was chosen because it is the highest Ru concentration for which XRD detects only bcc and no hcp reflections, and x = 20 was chosen because it is the lowest Ru concentration for which only hcp reflections are clearly detected. The results, presented and discussed in detail in Supplemental Material III [23], show that the crystal structure is unchanged after annealing.
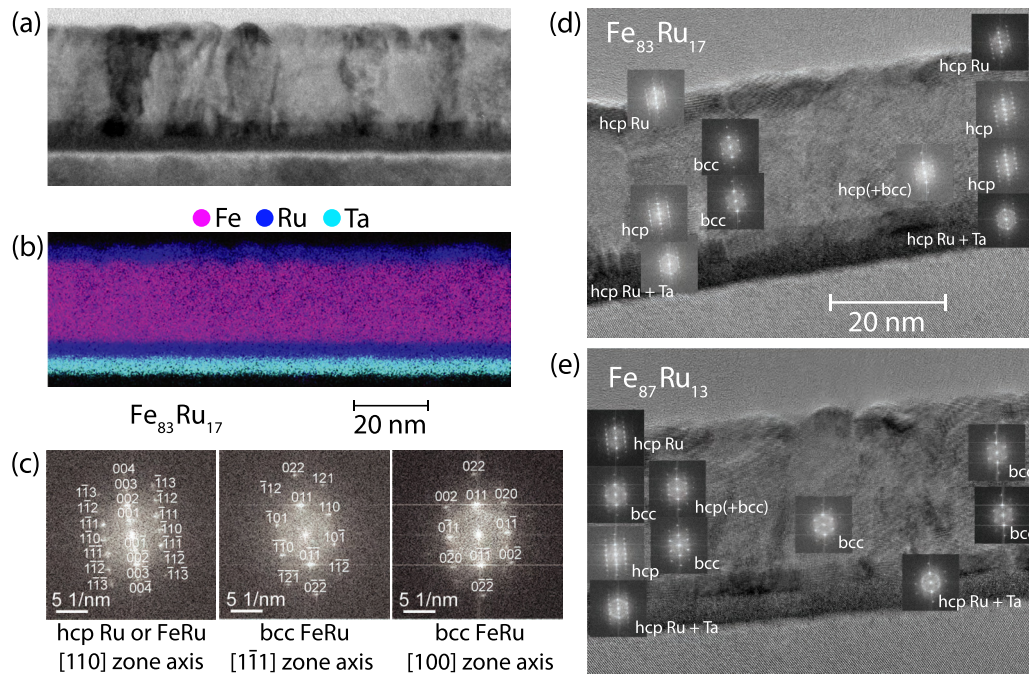
FIG. 4. (a) Bright-field transmission electron microscopy (TEM), and (b) STEM-EDXS-based element distribution images of Ta(3.5)|Ru(3.5)|Fe$_{83}$Ru$_{17}$(20)|Ru(3.5) with scale bar below, and (c) fast Fourier transform (FFT) patterns of hcp FeRu and Ru along the [110] zone axis and bcc FeRu along the [1$\bar{1}$1] and [100] zone axes. Example high-resolution TEM images of Ta(3.5)|Ru(3.5)|Fe$_{100-x}$Ru$_x$(20)|Ru(3.5) for (d) $x = 17$ and (e) $x = 13$ with scale bar in (d), including FFT patterns of various regions in the Ru and FeRu layers.

In the range from $x = 0$ to 8, additional in-plane and out-of-plane θ-2θ measurements were performed on as-deposited Ta|Ru|Fe$_{100-x}$Ru$_x$(100)|Ru. Figure 3 shows the 2θ value of the bcc Fe or FeRu {110} diffraction peak measured for these films and the corresponding lattice constant as a function of Ru concentration, x. Since Fe and Ru form a solid solution in this composition range and Ru atoms are larger than Fe atoms, an increase in Ru concentration leads to an increase in lattice constant. By Bragg's law, this translates to a decrease in the angle 2θ at which diffraction peaks are detected. As mentioned above, this effect is also visible in Fig. 1(b) as the Ru concentration increases from 23 to 50 at. %. Alongside the experimental 2θ and lattice constant values in Fig. 3 are two linear functions, both of which assume that Fe$_{100-x}$Ru$_x$ remains bcc for $0 \leqslant x \leqslant 8$. The bcc Ru interpolation, represented by the solid green line, is a linear function constructed from the following two points: the measured lattice constant of our Fe film obtained from the average of the in-plane and out-of-plane measurements ($x = 0$) and the lattice constant of a hypothetical bcc unit cell of Ru atoms with radius 0.1359 nm [30] ($x = 100$). The Fe$_{96}$Ru$_4$ extrapolation, represented by the dashed yellow line, is a linear function constructed from the average of the in-plane and out-of-plane measurements of our Fe film ($x = 0$) and our Fe$_{96}$Ru$_4$ film ($x = 4$). We used these two points because the equilibrium phase diagram shows that up to 4 at. % of Ru can be added to bcc Fe at elevated temperatures before the hcp lattice structure begins to appear [11]. The average of the measured lattice constants at $x = 8$ is larger than the lattice constant of both linear functions, indicating that Ru atoms are substituting Fe atoms in the bcc lattice up to at least 8 at. % of Ru in Fe. This is not unexpected, as films deposited by sputtering are likely not in equilibrium.

Furthermore, the out-of-plane and in-plane measurements in Fig. 3 yield similar results, indicating little difference in the lattice spacing for the two directions and suggesting that there is no distortion of the cubic structure.

B. Transmission electron microscopy

Cross-sectional TEM imaging was performed on Ta|Ru|Fe$_{100-x}$Ru$_x$(20)|Ru for $x = 13$ and 17 to identify the distribution of the bcc and hcp phases in FeRu. Fe$_{83}$Ru$_{17}$ was selected because it consists of a mixture of bcc and hcp FeRu, and Fe$_{87}$Ru$_{13}$ was selected because this alloy has the highest Ru concentration for which hcp diffraction peaks are not clearly detected in the XRD patterns, as evident from Fig. 2.

Figures 4(a) and 4(b) show a representative bright-field TEM image and the corresponding element distributions obtained by EDXS-based spectrum imaging analysis for Ta|Ru|Fe$_{83}$Ru$_{17}$(20)|Ru, respectively. The EDXS measurements confirm that the distribution of Fe and Ru in the FeRu film is homogeneous within measurement uncertainty. This suggests that the coexistence of the bcc and hcp phases in the FeRu films is not due to variation of the composition.

HRTEM images presented in Figs. 4(d) and 4(e) for Ta|Ru|Fe$_{83}$Ru$_{17}$(20)|Ru and Ta|Ru|Fe$_{87}$Ru$_{13}$(20)|Ru, respectively, are further analyzed by FFT analysis. The FFT patterns are placed on the HRTEM images at the locations at which they are calculated. Representative FFT patterns of hcp Ru and FeRu in [110] zone axis geometry and bcc FeRu in [1$\bar{1}$1] and [100] zone axis geometry are displayed separately in Fig. 4(c). In both films, the FFT patterns of Ru clearly show that Ru has hcp lattice structure, which is in agreement with the XRD measurements. FFT analysis also reveals that both FeRu films consist of grains that have entirely hcp and entirely

bcc crystal structure; furthermore, each film has indications of individual grains showing both phases. Since hcp diffraction peaks were not detectable in the XRD patterns of $Fe_{87}Ru_{13}$, it is evident that TEM analysis is more precise than XRD in detecting the presence of small amounts of a secondary phase.

We also performed cross-sectional TEM on Ta|Ru|Fe(100)|Ru to analyze the diffusion of Ru into the pure Fe film. The bright-field TEM and superimposed EDXS-based element distribution maps for a representative section of the sample are shown in Supplemental Material IV [23]. Quantifying the EDXS signal from the whole Fe layer, a Ru content of 0.1 at. % was determined. This could either be due to the diffusion of Ru into the Fe layer during the sputtering process or the introduction of Ru into the Fe layer during the TEM lamella preparation process. The bright-field TEM images in Fig. 4(a) and in Supplemental Material IV [23] show that the average grain diameter of our films is below 20 nm.

IV. MAGNETIC PROPERTIES

A. Mössbauer spectroscopy

Mössbauer measurements were used to study Ta|Ru|$Fe_{100-x}Ru_x$(100)|Ru films, with TMS performed on samples with $x = 0$, 4, and 8 at room temperature and CEMS performed on samples with $x = 13$, 18.5, 19.5, 23, and 50 at room temperature. Furthermore, CEMS was performed on Ta|Fe(100)|Ta, and CEMS and TMS were both performed on a single Fe(100) layer, all at room temperature. Additional TMS measurements of the single Fe(100) layer and of the Ta|Ru|$Fe_{100-x}Ru_x$(100)|Ru samples with $x = 0$, 4, and 8 were performed in the presence of a 0.166 T in-plane magnetic field, and TMS measurements of the samples with $x = 18.5$ and 19.5 were performed at 9.7 and 9.9 K, respectively.

For all measured films, the Mössbauer spectra were fitted to determine the isomer shift (IS), quadrupole splitting (QS), and hyperfine magnetic field (B_{HF}). Films with a cubic lattice structure have a QS of zero, and paramagnetic components of Mössbauer spectra have a B_{HF} of zero. The angle between the gamma ray (perpendicular to the film plane) and the average magnetization of the film, Φ_{MS}, was determined by comparing the peak intensities of the second and fifth lines with the other lines in the spectra. The intensities of the second and fifth lines depend only on the angle between the gamma ray (perpendicular to the film plane) and hyperfine field and are not affected by the in-plane orientation of the hyperfine field or the sign of the component of the hyperfine field along the gamma ray (parallel and antiparallel are equivalent). As a result, Mössbauer measurements yield the same angle if the out-of-plane magnetization components of the film are all pointing in the same direction as the gamma ray, all pointing in the opposite direction of the gamma ray, or any combination of the two. In contrast, vibrating sample magnetometry measurements with the external magnetic field applied perpendicular to the film normal treat these cases differently. In VSM measurements, the projections onto the field direction of all the magnetization components are summed, taking into account that projections in the same direction as the external magnetic field are positive and projections in the

TABLE I. Isomer shift (IS), quadrupole splitting (QS), hyperfine magnetic field (B_{HF}), angle between average magnetization and film normal (Φ_{MS}), and percentage of paramagnetic phase (PM) were extracted from Mössbauer spectroscopy measurements of the films in the left column. Films marked with § signify that the full structure is Ta(3.5)|Ru(3.5)|$Fe_{100-x}Ru_x$(100)|Ru(3.5). Rows marked with * indicate that the sample was measured via transmission Mössbauer spectroscopy, and rows without * were measured via conversion electron Mössbauer spectroscopy. Unless specified, each measurement was performed at room temperature and zero external magnetic field.

Film	IS (mm/s)	QS (mm/s)	B_{HF} (T)	Φ_{MS} (deg)	PM (%)
§$Fe_{50}Ru_{50}$	−0.047(2)	0.219(3)			100
§$Fe_{77}Ru_{23}$	−0.074(1)	0.188(2)			100
§$Fe_{80.5}Ru_{19.5}$	−0.07(1)	0.14(2)			100
§$Fe_{80.5}Ru_{19.5}$* (at 9.9 K)	0.044(2)	0.31(1)			100
§$Fe_{81.5}Ru_{18.5}$	0.028(1)		30.2(1)	40(2)	61(2)
	−0.072(1)	0.171(3)			
§$Fe_{81.5}Ru_{18.5}$* (at 9.7 K)	0.19(1)		32.3(6)	35(2)	65(1)
	−0.045(2)	0.30(1)			
§$Fe_{87}Ru_{13}$	0.037(4)		32.2(1)	45(1)	4(1)
	−0.37(2)	0.79(4)			
§$Fe_{92}Ru_8$*	0.027(3)		31.5(1)	44(1)	3.0(5)
§$Fe_{92}Ru_8$* (at 0.166 T)	0.032(3)		31.2(3)	47(1)	3.0(5)
§$Fe_{96}Ru_4$*	0.019(3)		31.9(1)	51(1)	2.5(7)
§$Fe_{96}Ru_4$* (at 0.166 T)	0.018(5)		32.9(3)	55(1)	2(1)
§Fe*	0.000(4)		32.83(3)	68(2)	0
§Fe* (at 0.166 T)	0.003(5)		32.61(4)	67(2)	0
Ta|Fe|Ta	0.007(1)		33.39(2)	73(1)	0
Fe	−0.003(1)		33.42(1)	80(1)	0
Fe*	−0.002(1)		33.13(1)	82(1)	0
Fe* (at 0.166 T)	−0.001(1)		32.38(1)	85(2)	0

opposite direction are negative (see Sec. IV B). For each film, we determined the percentage of paramagnetic phase (PM) by dividing the area under the central peak, which is the paramagnetic component of the spectrum, by the area under the entire spectrum. The five above-described parameters extracted from Mössbauer measurements—IS, QS, B_{HF}, Φ_{MS}, and PM—are tabulated in Table I for all films measured by Mössbauer spectroscopy.

Table I shows that Ta|Ru|$Fe_{100-x}Ru_x$(100)|Ru is fully paramagnetic for $x \geqslant 19.5$, as indicated by PM being 100 % and B_{HF} being absent. This can be visualized in the CEMS measurements in Fig. 5, which show one central peak for $x = 19.5$, 23, and 50. When compared with the XRD measurements, it follows that hcp FeRu is paramagnetic at room
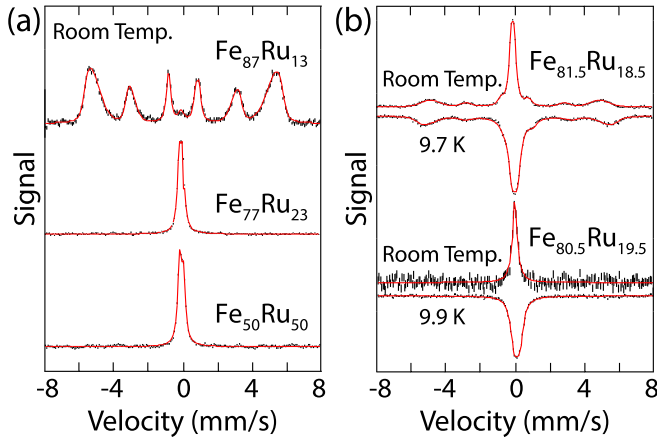
FIG. 5. (a) Conversion electron Mössbauer spectroscopy (CEMS) measurements at room temperature of $Ta(3.5)|Ru(3.5)|Fe_{100-x}Ru_x(100)|Ru(3.5)$ for $x = 13$, 23, and 50 and (b) CEMS measurements at room temperature and transmission Mössbauer spectroscopy (TMS) measurements at low temperature of $Ta(3.5)|Ru(3.5)|Fe_{100-x}Ru_x(100)|Ru(3.5)$ for $x = 18.5$ and 19.5. All measurements are performed at zero external magnetic field.

temperature. When the Ru concentration decreases from 19.5 to 18.5 at. %, B_{HF} appears and the percentage of paramagnetic phase in the film drops from 100 to 61 %. The mixture of the paramagnetic and magnetic phase in $Fe_{81.5}Ru_{18.5}$ can also be seen in the CEMS measurements in Fig. 5(b). At this concentration, B_{HF} is 30.2 ± 0.1 T, which is already about 90 % of the hyperfine field known for pure Fe, 33 T [31]. As the Ru concentration in $Fe_{100-x}Ru_x$ decreases further from 18.5 to 13 at. %, B_{HF} increases to 32.2 ± 0.1 T and only 4 % of the film is paramagnetic. The small percentage of paramagnetic phase remaining in the film is indicated by the small central peak in the CEMS measurements of $Fe_{87}Ru_{13}$ in Fig. 5(a). Though the presence of the hcp phase in $Fe_{87}Ru_{13}$ was not detected by XRD, it was detected by the more precise method, TEM, confirming that the paramagnetic contribution observed by Mössbauer spectroscopy is due to the hcp FeRu phase. Mössbauer spectroscopy also shows that films for which the magnetic phase is detected, i.e., $Fe_{100-x}Ru_x$ with $x \leqslant 18.5$, have an average magnetization that is tilted out of the film plane. The average magnetization angle from the film normal, Φ_{MS}, does not change significantly until the Ru concentration is less than 8 at. %. For $Fe_{81.5}Ru_{18.5}$, CEMS measurements give $\Phi_{MS} = 40 \pm 2°$ from the film normal. For $Fe_{87}Ru_{13}$, CEMS measurements yield $\Phi_{MS} = 45 \pm 1°$, and for $Fe_{92}Ru_8$, TMS measurements give $\Phi_{MS} = 44 \pm 1°$.

When $Fe_{81.5}Ru_{18.5}$ is cooled to 9.7 K, B_{HF} of the magnetic phase increases from 30.2 ± 0.1 to 32.3 ± 0.6 T, but the percentages of the paramagnetic and magnetic phases remain practically the same [see Table I and Fig. 5(b)]. Additionally, Table I and Fig. 5(b) show that $Fe_{80.5}Ru_{19.5}$ remains fully paramagnetic when cooled to 9.9 K, indicating that $Fe_{100-x}Ru_x$ is paramagnetic above 9.9 K for $x \geqslant 19.5$.

The TMS measurements of $Ta|Ru|Fe_{100-x}Ru_x(100)|Ru$ for $x = 4$ and 8 in Fig. 6(a) show that these films have only a trace of the paramagnetic phase, which disappears for $x = 0$. This is confirmed by the percentage of paramagnetic phase tabulated in Table I. Comparing these results with the XRD
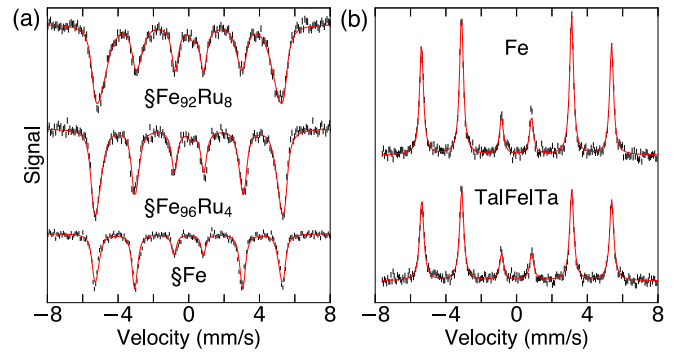

FIG. 6. (a) Transmission Mössbauer spectroscopy (TMS) measurements of $Ta(3.5)|Ru(3.5)|Fe_{100-x}Ru_x(100)|Ru(3.5)$ for $x = 0$, 4, and 8 and (b) conversion electron Mössbauer spectroscopy (CEMS) measurements of Fe(100) (no surrounding layers) and $Ta(3.5)|Fe(100)|Ta(3.5)$. All measurements are performed at room temperature and zero external magnetic field.

measurements, we can confirm that bcc Fe and FeRu are magnetic. Since the magnetic phase has cubic structure (bcc), quadrupole splitting is zero for $x \leqslant 8$. Table I shows that the hyperfine field increases as x decreases from 8 to 0 at. % of Ru in Fe and reaches approximately 33 T, the hyperfine field previously measured for pure Fe [31]. In the same Ru concentration range, the average magnetization direction moves towards the plane, as seen in Table I. For $x = 8$, TMS measurements give an angle of $\Phi_{MS} = 44 \pm 1°$ from the film normal. For $x = 4$, Φ_{MS} increases to $51 \pm 1°$, and for $x = 0$, Φ_{MS} increases further to $68 \pm 2°$ from the film normal. This result for $Ta|Ru|Fe(100)|Ru$ is very unexpected. Due to the relatively small magnetocrystalline anisotropy of bcc Fe as compared to the large in-plane shape anisotropy of the studied Fe films, the magnetization is expected to lie in the plane. The large shape anisotropy arises from the large M_s of the studied Fe films. One possible explanation of the out-of-plane magnetization components measured in $Ta|Ru|Fe(100)|Ru$ is the presence of a very small amount of Ru in the Fe film. Quantification of the STEM-EDXS analysis of this film (Supplemental Material IV [23]) indicates that the Fe layer may contain up to 0.1 at. % of Ru.

To eliminate any contribution from Ru in the Fe film, CEMS was performed on a 100-nm-thick Fe film surrounded only by 3.5 nm-thick Ta, and CEMS and TMS were both performed on a single 100-nm-thick Fe layer. The parameters of these three measurements are presented in Table I, and the CEMS measurements of both films are displayed in Fig. 6(b). The hyperfine fields for both films are approximately 33 T, in agreement with the hyperfine field known for Fe [31]. However, the average magnetization direction as compared to that of $Ta|Ru|Fe|Ru$ moves closer to the plane for $Ta|Fe|Ta$ ($\Phi_{MS} = 73 \pm 1°$ from the normal), and closer still for the single Fe layer ($\Phi_{MS} = 80 \pm 1°$ from CEMS and $82 \pm 1°$ from TMS). Since domain walls have out-of-plane magnetization components that could be responsible for these observations, an in-plane magnetic field of 0.166 T was applied to the single Fe layer to expel all domains and TMS was again performed. As a result of the application of the magnetic field, Φ_{MS} of the single Fe layer only increased to $85 \pm 2°$ from the film normal, showing that the presence of domain walls
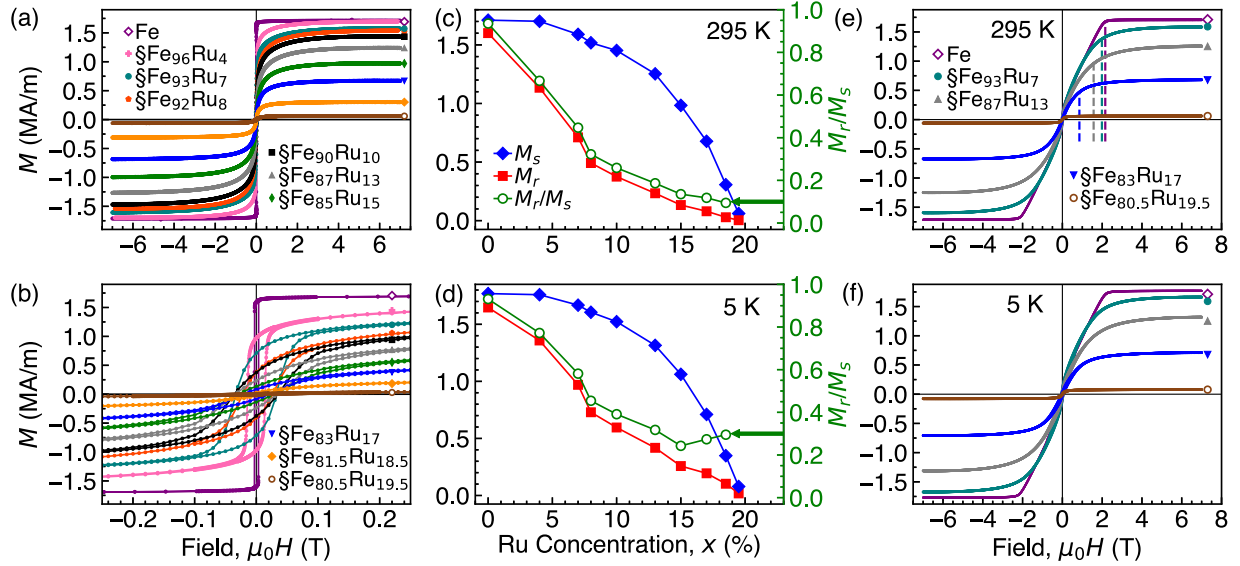
FIG. 7. $M(H)$ measurements with magnetic field applied parallel to the film surface over (a) the full measured field range and (b) a zoomed-in field range to highlight the hysteresis loops of as-deposited Fe(100), §Fe$_{100-x}$Ru$_x$(100) for $x = 4$ and 8, and §Fe$_{100-x}$Ru$_x$(20) for $x = 7$, 10, 13, 15, 17, 18.5, and 19.5, where § signifies that the full structure is Ta(3.5)|Ru(3.5)|Fe$_{100-x}$Ru$_x$(d)|Ru(3.5). M_s, M_r, and M_r/M_s from the $M(H)$ measurements in (a) and (b) are plotted at (c) 295 and (d) 5 K. $M(H)$ measurements with magnetic field applied perpendicular to the film surface of as-deposited Fe(100) and §Fe$_{100-x}$Ru$_x$(20) for $x = 7$, 13, 17, and 19.5 at (e) 295 and (f) 5 K. The dashed lines in (e) represent the calculated demagnetizing fields for Fe(100) and §Fe$_{100-x}$Ru$_x$(20) ($7 \leqslant x \leqslant 17$) films.

only changes the average magnetization direction by a few degrees. For confirmation, we also measured Ta|Ru|Fe$_{100-x}$Ru$_x$(100)|Ru for $x = 0$, 4, and 8 with TMS in the presence of the 0.166 T in-plane magnetic field and, as with the single Fe layer, the removal of magnetic domains only changed Φ_{MS} by a few degrees.

B. Vibrating sample magnetometry

VSM measurements were used to determine the magnetization of Ta|Ru|Fe$_{100-x}$Ru$_x$(d)|Ru ($0 \leqslant x \leqslant 19.5$), Ta|Fe(100)|Ta, and Fe(100) films as a function of an external magnetic field applied either parallel or perpendicular to the film surface and at a temperature of 5 or 295 K. From the measurements, we obtained the saturation magnetization, M_s, and the remanent magnetization along the field direction, M_r. The remanent-to-saturation magnetization ratio, M_r/M_s, allows us to infer information about the magnetic structure of the Fe$_{100-x}$Ru$_x$ films. Additionally, for selected structures, we found the external magnetic field above which the magnetization is reversible, H_{rev}. Above this field, domains are expelled from the film and do not contribute to the $M(H)$ measurements.

Figures 7(a) and 7(b) show the $M(H)$ measurements at 295 K of Fe(100), Ta|Ru|Fe$_{100-x}$Ru$_x$(100)|Ru for $x = 4$ and 8, and Ta|Ru|Fe$_{100-x}$Ru$_x$(20)|Ru for $x = 7$, 10, 13, 15, 17, 18.5, and 19.5, with the magnetic field applied parallel to the film surface (referred to as in plane). M_r, M_s, and the M_r/M_s ratio for each film are plotted as a function of Ru concentration in Figs. 7(c) and 7(d) at 295 and 5 K, respectively.

It can be seen in Fig. 7(c) that M_s decreases with Ru concentration from 1711 kA/m for the single Fe layer to 61 kA/m for Fe$_{80.5}$Ru$_{19.5}$ at room temperature. M_s decreases slowly

over the $0 \leqslant x \leqslant 10$ composition range of Fe$_{100-x}$Ru$_x$ and sharply for $13 \leqslant x \leqslant 19.5$. On the other hand, M_r sharply decreases with x up to 8 at. % and decreases at a lower rate for larger x; the M_r/M_s ratio follows the same trend as M_r.

The M_s measurements at 5 K in Fig. 7(d) are slightly higher than those at 295 K for all plotted Ru concentrations, as expected for ferromagnetic materials [32]. Figure 7(d) also shows that if the ambient temperature is decreased from 295 K to 5 K, M_r stays practically the same for the single Fe layer but increases for all FeRu alloys. Consequently, the M_r/M_s ratio also increases. The increase is most significant for the films with the highest Ru concentrations.

From Figs. 7(a) and 7(b), it is evident that the field required to saturate the FeRu alloys is much higher than that required to saturate the pure Fe film. Large saturation fields are observed even for very low concentrations of Ru in Fe. To highlight the approach to saturation, Fig. 8(a) shows the normalized $M(H)$ curves for $H \geqslant 0$ of Fe(100) and of Ta|Ru|Fe$_{100-x}$Ru$_x$(100)|Ru for $x = 0$, 4, and 8. Even for Ta|Ru|Fe(100)|Ru, the field required to saturate the magnetization is significantly larger than that required for the single Fe layer with no surrounding layers. This could be due to Ru diffusing into the Fe layer, which is suggested by the TEM-based analysis in Supplemental Material IV [23].

Marked on each $M(H)$ curve in Fig. 8(a) with a cyan diamond is the point at which the magnetization becomes reversible with the magnetic field, $M(H_{rev})$, meaning that all the magnetic domains have been expelled from the film. Magneto-optical microscopy measurements in Sec. IV C confirm that there are no domains for $H \geqslant H_{rev}$. These points are also indicated in Fig. 8(b), which shows the $M(H)$ loops of the same films in Fig. 8(a). As the Ru concentration in the film increases, the field required to expel the domains increases;
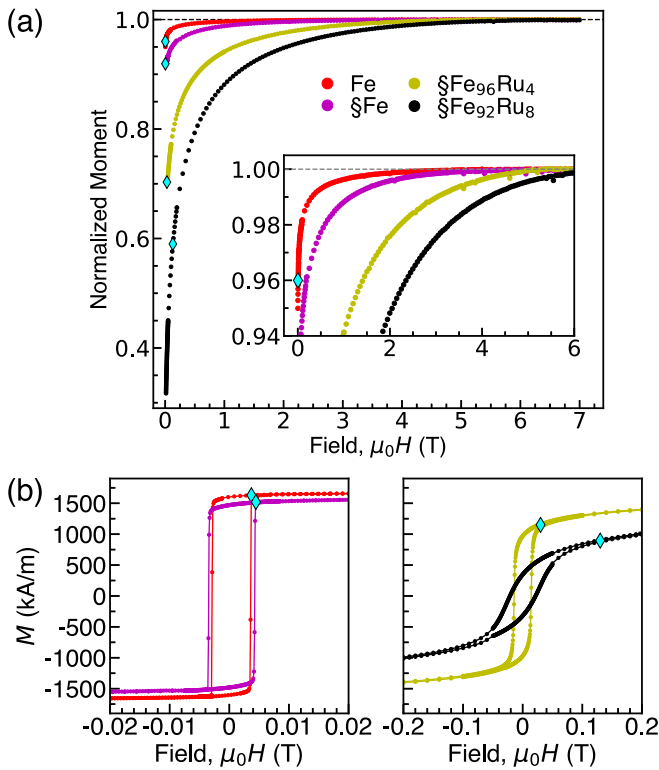
FIG. 8. (a) $M(H)/M_s$ and (b) $M(H)$ measurements with magnetic field applied parallel to the film surface of as-deposited Fe(100) and of Ta(3.5)|Ru(3.5)|Fe$_{100-x}$Ru$_x$(100)|Ru(3.5) for $x = 0$, 4, and 8, where the § in the legend signifies that the layer is grown on top of Ta|Ru and capped with Ru. The magnified inset plot in (a) highlights the variation in saturation field. The magnetic field ranges in (b) are chosen to highlight the hysteresis loops of the samples. Cyan diamonds are placed at the lowest field for which the hysteresis loop is reversible, indicating the removal of magnetic domains.

FIG. 9. MOKE microscopy image of the Ta|Ru|Fe$_{96}$Ru$_4$(100)|Ru film surface with (a) 14.3 mT and (b) 30 mT applied parallel to the film surface. Small domains that are elongated along the film direction are visible at 14.3 mT, and no domains are visible at 30 mT. (c) $M(H)$ loop of Ta|Ru|Fe$_{96}$Ru$_4$(100)|Ru, which is also plotted in Fig. 8(b). Dashed lines are placed at the field values that correspond with (a) and (b).

however, in each case, the domains are expelled in fields lower than 0.13 T.

Figure 7(e) shows the $M(H)$ measurements of as-deposited Fe(100) and Ta|Ru|Fe$_{100-x}$Ru$_x$(20)|Ru for $x = 7$, 13, 17, and 19.5 at 295 K, with the magnetic field applied perpendicular to the film plane (referred to as perpendicular-to-plane). Fe and all the FeRu alloys have an M_r/M_s of nearly zero, indicating that the net projection of magnetic moments along the field direction is nearly zero when the field is removed.

The field required to saturate the magnetization of the single Fe layer perpendicular to the film plane is slightly larger than the shape anisotropy or demagnetizing field, $\mu_0 M_s = 2.15$ T, which is represented by the rightmost dashed line (purple) in Fig. 7(e). In addition to shape anisotropy, Fe films have a much smaller magnetocrystalline anisotropy, which is oriented along the $\langle 100 \rangle$ directions. The magnetocrystalline anisotropy field contributes to the field required to saturate the sample. When 7 to 17 at. % of Ru is added to the Fe film, the saturation fields for the perpendicular-to-plane measurements increase to above 6 T, which is several times larger than the demagnetizing fields of the films [represented by the additional dashed lines in Fig. 7(e)]. The perpendicular-
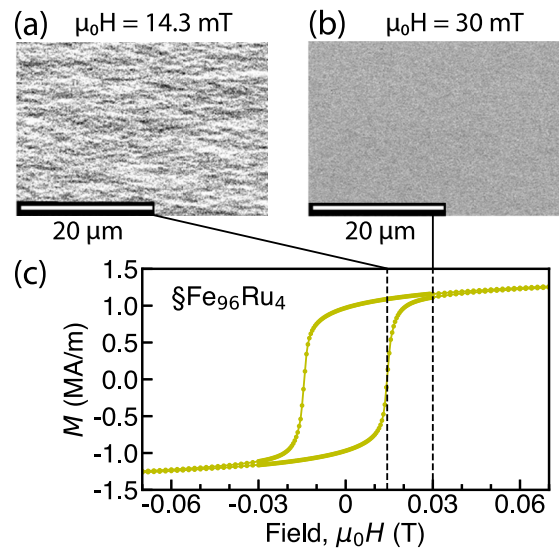
to-plane $M(H)$ measurements performed at 5 K, presented in Fig. 7(f), are very similar to those performed at 295 K.

C. Magneto-optical Kerr effect microscopy

MOKE microscopy measurements were performed on Ta|Ru|Fe$_{96}$Ru$_4$(100)|Ru to observe how the domain structure of the film evolves in an in-plane applied magnetic field. Initially, a magnetic field of -1.1 T was applied in the film plane, saturating the magnetic moments along the field direction. The field was subsequently removed and then swept up to 1.1 T while the domain structure was observed. Figure 9(a) presents the MOKE microscopy image of Ta|Ru|Fe$_{96}$Ru$_4$(100)|Ru at an applied field of 14.3 mT. For reference, the $M(H)$ loop of the film, Fig. 9(c), is placed below the image. At 14.3 mT, the coercive field of the film, small domains textured along the field direction were observed. When the magnetic field reached 30 mT, the domains were entirely expelled, as can be seen in Fig. 9(b). This field coincides with the point marked by a diamond in Fig. 8 at which the $M(H)$ loop of the Fe$_{96}$Ru$_4$ sample becomes reversible. Therefore, the reversible parts of our $M(H)$ loops are not affected by domains. The texture of the domains follows the direction of the applied magnetic field, suggesting that the film is isotropic within the plane, i.e., there is no preferred magnetic anisotropy direction in the plane. The observed pattern is neither purely stripe nor ripple domain structure, but rather a domain structure typical of polycrystalline magnetic films with magnetocrystalline anisotropy that is averaged out of the film plane.

D. Lorentz transmission electron microscopy

The magnetization reversal process of a Ta|Ru|Fe$_{92}$Ru$_8$(20)|Ru film was investigated in more detail by LTEM, which is able to probe the in-plane magnetization orientation at the nanoscale. The sample was tilted by a tilt angle θ with respect to the film normal, and a magnetic field of H_{appl} was applied, yielding an in-plane magnetic field of $H_{IP} = H_{appl} \sin \theta$ and an out-of-plane magnetic field of $H_{OOP} = H_{appl} \cos \theta$.

Prior to acquiring images, the sample was tilted by $-40°$ with respect to the film normal in an applied magnetic field of about 2 T to align the in-plane magnetization of the sample toward the negative direction. Subsequently, H_{appl} was reduced to zero to bring the in-plane magnetization to the negative remanence point. Images were then acquired at room temperature with the sample tilted at $\theta = +40°$, beginning at the negative remanence point and increasing H_{appl} in steps up to 2 T. It is important to point out that, by tilting the sample by $+40°$, the LTEM contrast is more enhanced than that of the zero tilt case (images not shown), which is consistent with the average magnetization angle measured by Mössbauer spectroscopy of $44 \pm 1°$ from the film normal in the absence of an external magnetic field.

Figure 10(a) shows the magnetic domain structure at zero magnetic field, revealing that the size of the magnetic features in Fe$_{92}$Ru$_8$ is similar to the grain diameter of our films (determined by the bright-field TEM images in Fig. 4(a) and Supplemental Material IV [23]). By increasing the applied magnetic field H_{appl} from zero to 144 mT (i.e., $H_{IP} = 92.6$ mT and $H_{OOP} = 110.3$ mT), individual switching events can be seen [Figs. 10(a)–10(d)]. The switching events are more clear in the corresponding contrast difference images presented in Figs. 10(e) and 10(f). The small reversed areas are most likely noncollinear spin clusters arising from the competing ferromagnetic and antiferromagnetic interactions between the magnetic Fe atoms, as will be discussed in Sec. V B. Switching events in the film can also be observed in the video provided in Supplemental Material V [23], in which the sample is tilted at $\theta = 20°$ and H_{appl} is increased from 96 to 112 mT.

At higher magnetic fields, up to $H_{appl} = 2$ T, only a few individual switching events were observed (images not shown). Furthermore, the overall LTEM contrast is reduced, implying that the magnetization is predominantly oriented along the applied magnetic field direction. This is consistent with Fig. 8(b), which shows that the magnetization of Ta|Ru|Fe$_{92}$Ru$_8$(20)|Ru is reversible at in-plane fields above 130 mT.

V. DISCUSSION

A. Experimental results

The structural measurements, XRD and TEM, show that the studied films are polycrystalline with grains that are randomly oriented in the plane of the film. The grains with bcc crystal structure are textured along the growth direction, $\langle 110 \rangle$, and the grains with hcp crystal structure are textured along the $\langle 001 \rangle$ directions. For Ta|Ru|Fe$_{100-x}$Ru$_x$|Ru films, Fe$_{100-x}$Ru$_x$ rocking curve measurements show that the full
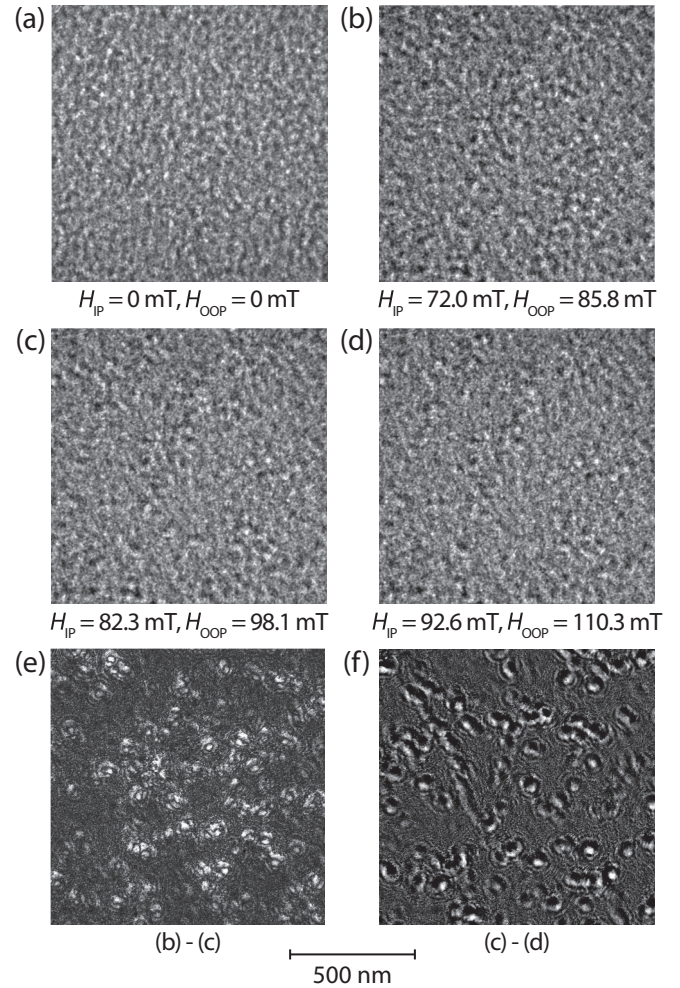

$H_{IP} = 0$ mT, $H_{OOP} = 0$ mT

$H_{IP} = 72.0$ mT, $H_{OOP} = 85.8$ mT

$H_{IP} = 82.3$ mT, $H_{OOP} = 98.1$ mT

$H_{IP} = 92.6$ mT, $H_{OOP} = 110.3$ mT

(b) - (c)

(c) - (d)

500 nm

FIG. 10. (a)–(d) Lorentz transmission electron microscopy images taken at the same location on a Ta(3.5)|Ru(3.5)|Fe$_{92}$Ru$_8$(20)|Ru(3.5) film as the applied magnetic field is increased. The in-plane and out-of-plane applied magnetic field values are below the images. (e), (f) Contrast difference images showing all the switching events that occurred due to the field increase written below the image. The scale bar at the bottom applies to all images. All images are taken at room temperature with a defocus of -1 mm and a tilt angle of $+40°$.

width at half maximum is 2.6° or below for films grown on Si and 6.1° or below for films grown on Kapton (see Supplemental Material II [23]).

The XRD and TEM measurements indicate that room-temperature Fe$_{100-x}$Ru$_x$ transitions from bcc to hcp crystal structure as x increases from ~ 13 at. % to ~ 20 at. %. Our Mössbauer spectroscopy measurements show no magnetic order in Fe$_{100-x}$Ru$_x$ films with $x \geqslant 19.5$, while films with $x \leqslant 13$ are at least 96 % magnetic. Combining these measurements with the structural measurements suggests that hcp FeRu is paramagnetic and bcc FeRu is magnetic. From the TEM measurements, we also observed that the Fe$_{87}$Ru$_{13}$ and Fe$_{83}$Ru$_{17}$ films consist of grains having entirely hcp or entirely bcc lattice structure; furthermore, each film has indications of individual grains showing both phases. STEM-EDXS

analysis of the Ta|Ru|Fe$_{100-x}$Ru$_x$|Ru structure reveals a uniform distribution of Ru throughout the FeRu films.

XRD measurements show that the lattice expansion with the addition of Ru to Fe is linear for up to 8 at.% of Ru in Fe, indicating that Ru atoms substitute Fe atoms in the bcc crystal lattice. Out-of-plane and in-plane XRD measurements of Fe$_{100-x}$Ru$_x$ for $0 \leqslant x \leqslant 8$ indicate no difference in the lattice spacing for the in-plane and out-of-plane directions, suggesting that the cubic structure is not distorted by the addition of Ru.

MOKE microscopy measurements show that magnetic domains are entirely expelled in the reversible part of the $M(H)$ loop. The field at which the $M(H)$ loop becomes reversible, H_{rev}, increases from 0.0037 T for the single Fe layer to 0.13 T for Ta|Ru|Fe$_{92}$Ru$_8$|Ru. The MOKE measurements also show that the domain pattern present in our films is neither stripe nor ripple. Comparing the MOKE microscopy measurements of Fe$_{96}$Ru$_4$ and LTEM measurements of Fe$_{92}$Ru$_8$ reveals that increasing the Ru concentration in bcc FeRu decreases the size of the magnetic domains, making it comparable to the grain diameter.

In the absence of an external magnetic field, the angle of the average magnetization with respect to the film normal measured by Mössbauer spectroscopy, Φ_{MS}, of Ta|Ru|Fe$_{100-x}$Ru$_x$|Ru increases from $40 \pm 2°$ for $x = 18.5$, to $51 \pm 1°$ for $x = 4$, and to $68 \pm 2°$ for $x = 0$. For a single layer of Fe with no surrounding layers, Φ_{MS} increases to $82 \pm 1°$. Since domain walls can have out-of-plane magnetization components, Φ_{MS} was also measured in the presence of a 0.166 T external magnetic field to expel all magnetic domains in the film. With the field applied, Φ_{MS} increased slightly to $55 \pm 1°$ for $x = 4$ and to $85 \pm 2°$ for the single Fe layer. Therefore, magnetization in domain walls does not contribute significantly to the out-of-plane magnetization component. A discussion of the small out-of-plane component observed in the single Fe layer is presented in Supplemental Material VI [23].

The room-temperature $M(H)$ measurements of the Fe$_{100-x}$Ru$_x$ films with the magnetic field applied parallel to the film plane show that M_s initially decreases slowly with x up to 10 at.%, which is predominantly due to Ru atoms substituting Fe atoms in the host bcc lattice. The decrease in M_s agrees with the small decrease in the hyperfine field measured by Mössbauer spectroscopy over this composition range. For $13 \leqslant x \leqslant 19.5$, M_s sharply decreases to 0, which is mainly due to magnetic bcc FeRu transforming into paramagnetic hcp FeRu. This is corroborated by our Mössbauer measurements in this composition range, which show a large increase in the percentage of paramagnetic phase in the film (from 4% to 100%) and only a small change in the hyperfine field. On the other hand, the remanent-to-saturation magnetization ratio, M_r/M_s, sharply decreases with x up to 8 at.% and decreases at a lower rate for larger x, indicating that the magnetic moments at zero field deviate more from the field direction for larger Ru concentrations. This trend correlates with the increase in the out-of-plane magnetization component observed by Mössbauer spectroscopy, i.e., the decrease in the angle Φ_{MS} with respect to the film normal. The M_r/M_s measurements of the Fe$_{100-x}$Ru$_x$ films at 5 K are similar to those at room temperature except for $x \geqslant 17$, for which M_r/M_s increases due to the increase in the magnetic order of the structure.

The $M(H)$ measurements of the Fe$_{100-x}$Ru$_x$ films with the field applied perpendicular to the plane have a very small magnetization along the film normal at zero field for all measured compositions. Combining these results with the out-of-plane magnetization detected by Mössbauer spectroscopy, we conclude that Fe$_{100-x}$Ru$_x$ films with $x \leqslant 18.5$ have out-of-plane magnetization components pointing both up and down along the film normal that almost fully cancel each other out. This is expected, as the demagnetizing field in the film is reduced when the net magnetization along the film normal is zero.

When a very large magnetic field is applied in the plane of a film, the magnetic moments lie along the field direction, producing a net magnetization of M_s in the field direction. As the field is reduced to zero, the magnetic moments may deviate from the field direction, resulting in a remanent magnetization along the field direction of $M_r \leqslant M_s$. Therefore, the ratio M_r/M_s provides information on the distribution of magnetic moments in the film in the absence of an external magnetic field. Supplemental Material VII [23] provides magnetic moment distributions and calculations of M_r/M_s for ferromagnetic films after a large in-plane magnetic field is removed. The films considered there have noninteracting magnetic grains with easy axes randomly oriented in all directions. If the demagnetizing field or in-plane shape anisotropy of the film is neglected, M_r/M_s is calculated to be 0.5. If the film has a demagnetizing field that is much larger than the magnetocrystalline anisotropy field of the magnetic grains, all the magnetic moments lie in the plane at zero field and M_r/M_s increases to 0.64. In cases where there is a strong direct exchange interaction between the grains, as in our Fe$_{100-x}$Ru$_x$ films, the magnetic moments are pulled toward each other, significantly increasing M_r/M_s. This is corroborated by our single Fe layer, for which M_r/M_s of the in-plane $M(H)$ measurements is 0.94. On the contrary, $M_r/M_s < 0.4$ for our films with $x \geqslant 8$, suggesting that our magnetic FeRu films are not ferromagnetic (i.e., the magnetic interactions do not cause the magnetic moments of Fe atoms to align with each other).

The field required to saturate the magnetic moments of ferromagnetic materials along the direction of the external field, the saturation field, can be calculated as $2K_1/M_s$, where K_1 is the first anisotropy constant and M_s is the saturation magnetization of the ferromagnetic material [32]. Here, we assume $K_2 = K_3 = 0$ and neglect the demagnetizing fields. For pure Fe, $K_1 = 48 \, \mathrm{kJ/m^3}$ [32], resulting in a saturation field of 0.056 T. Since the magnetic phase of FeRu has a cubic crystal structure (bcc) and no structural distortion is observed for Fe$_{100-x}$Ru$_x$ films with $x \leqslant 8$, K_1 is small, resulting in a relatively small saturation field. The observed saturation fields in our FeRu films are two orders of magnitude larger than that of Fe, again suggesting that our films are not ferromagnetic.

Furthermore, our samples have a large M_s, exceeding 1.5 MA/m for Fe$_{100-x}$Ru$_x$ with $x \leqslant 8$, which induces a large in-plane shape anisotropy in our films. Due to the small magnetocrystalline anisotropy of the magnetic phase of FeRu, it is expected that the shape anisotropy will force the magnetization of the film to lie in the film plane. On the contrary, from Mössbauer measurements, the average magnetization is

aligned at an angle between $39°$ and $50°$ out of the film plane (i.e., Φ_{MS} between $51°$ and $40°$) for $x \geqslant 4$ at room temperature. Even in the presence of an external magnetic field large enough to expel all domains, the average magnetization was at an angle of at least $35°$ out of the film plane for $x \geqslant 4$. This clearly shows that magnetization in domain walls is not responsible for the observed out-of-plane magnetization component. Thus, the out-of-plane magnetization component is another indication that our films do not have ferromagnetic alignment.

The low M_r/M_s, high saturation field, and presence of an out-of-plane magnetization component observed in our magnetic FeRu films can be explained by noncollinear alignment between magnetic Fe atoms within the films. This noncollinear alignment, combined with the sub-20 nm grain microstructure of our films, gives rise to the nanogranular magnetic domain structure observed by LTEM.

B. Atomistic model

The recently developed atomistic model [33] was successfully used to simulate the magnetic coupling of Co layers across FeRu layers. In the model, the crystal structure is simplified to simple cubic with a lattice constant of $a = 0.25$ nm. Neighboring Fe atoms couple ferromagnetically due to the direct exchange interaction, while two Fe atoms separated by one or more Ru atoms couple antiferromagnetically due to the indirect Ruderman-Kittel-Kasuya-Yosida (RKKY) exchange interaction. The model only includes ferromagnetic and antiferromagnetic couplings between pairs of Fe atoms along the three principal axes of the simple cubic unit cell. Further details about the atomistic model can be found in Refs. [33,34].

We used the atomistic model to simulate $Fe_{100-x}Ru_x$ films for $0 \leqslant x \leqslant 10$, using a saturation magnetization of $M_s = 1700$ kA/m to obtain the dipole moment of the Fe atoms and an exchange stiffness of $A_{ex} = 21$ pJ/m to obtain the Heisenberg exchange constant between the Fe atoms. The antiferromagnetic coupling strengths of Fe across one, two, and three Ru atoms are -3.13×10^{-21}, -1.14×10^{-21}, and -4.43×10^{-22} J, respectively. To account for the large shape anisotropy in our $Fe_{100-x}Ru_x$ films, we introduced a demagnetizing field, with the easy-plane shape anisotropy being $K_{shape} = -\mu_0 M_s^2/2$. Figure 11(a) shows the magnetic moment distribution in the $Fe_{90}Ru_{10}$ film after a large magnetic field is applied along the x axis, parallel to the film plane, and then reduced to zero. The complex configuration is caused by the competition between the ferromagnetic and antiferromagnetic couplings between the Fe atoms. The vast majority of magnetic moments have a positive projection along the magnetic field direction after the field is removed, and for this reason, the color of the magnetic moments with a negative projection is kept the same in Fig. 11(a).

From the magnetic moment distribution of the $Fe_{90}Ru_{10}$ film, we calculated the average projection of the normalized magnetic moments on the x axis (the field direction), the y axis, and the z axis (the film normal) as a function of the external magnetic field, as shown in Fig. 11(b). Since the magnetic field is applied along the x axis, the magnetic moments preferentially point in the positive x direction, as
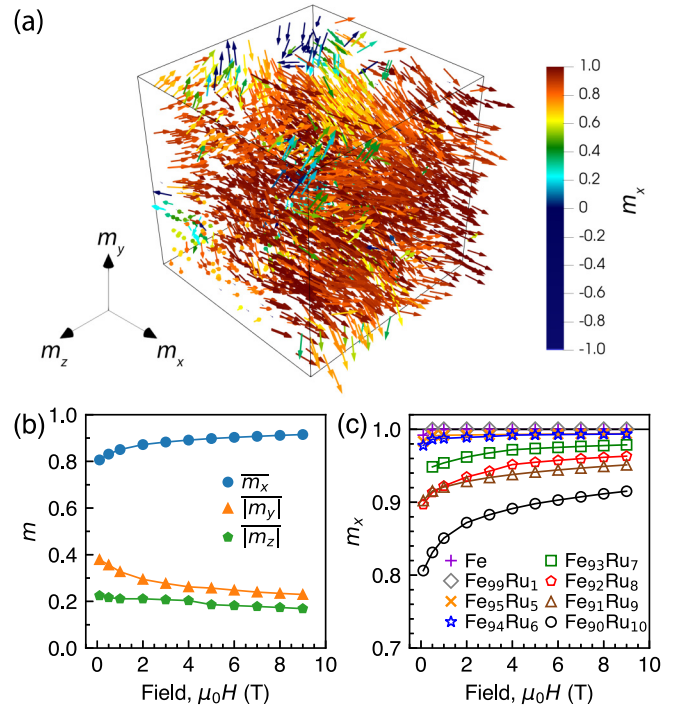

FIG. 11. (a) Simulated magnetic moment distribution of an $Fe_{90}Ru_{10}$ film after magnetic field along x axis is removed. (b) For the same film, average projection of normalized magnetic moments along x axis (field direction) and average absolute value projections along y axis and z axis (film normal) as a function of applied magnetic field. (c) Simulated normalized in-plane $M(H)$ dependence of $Fe_{100-x}Ru_x$ films ($0 \leqslant x \leqslant 10$).

expected; in fact, $\overline{m_x} \geqslant 0.8$ for all fields greater than or equal to 0.1 T. However, the magnetic moments have no analogous preferential direction along the y axis or z axis, causing the average projection on these two axes to be zero. For this reason, we have plotted the average of the absolute value of the normalized magnetic moment projections along the y and z directions, $\overline{|m_y|}$ and $\overline{|m_z|}$, respectively. Figures 11(a) and 11(b) both show that there is a substantial magnetization component in the z direction, perpendicular to the film plane. This can explain the out-of-plane magnetization component observed by Mössbauer spectroscopy.

In Fig. 11(c), the average projection of the normalized magnetic moments along the field direction, $\overline{m_x}$, is plotted as a function of external magnetic field for 100-nm-thick $Fe_{100-x}Ru_x$ films in the concentration range $0 \leqslant x \leqslant 10$. These curves correspond with our normalized $M(H)$ curves measured by VSM. Figure 11(c) shows a decreasing trend in M_r/M_s with increasing Ru concentration in Fe that agrees with our measurements in Figs. 7 and 8. Additionally, Fig. 11(c) shows that a large field is required to fully saturate the films, as shown in Fig. 8(a). However, the simulated decrease in M_r/M_s is much slower than the experimental decrease in M_r/M_s, and the saturation fields are much larger.

VI. CONCLUSION

In summary, we have studied the structural and magnetic properties of sputter-deposited $Fe_{100-x}Ru_x$ films by

means of x-ray diffraction (XRD), transmission electron microscopy (TEM), Mössbauer spectroscopy, vibrating sample magnetometry (VSM), magneto-optical Kerr effect (MOKE) microscopy, and Lorentz transmission electron microscopy (LTEM). All studied films are polycrystalline and exhibit texture along the growth direction. The crystal structure of the $Fe_{100-x}Ru_x$ films is predominantly bcc for $x < 13$ and undergoes a gradual transition to hcp in the concentration range $13 \lesssim x \lesssim 20$. Within this transitional range, the films consist of grains that have fully bcc, fully hcp, and a mixture of bcc and hcp lattice structure.

While Fe has ferromagnetic order, the addition of Ru introduces a noncollinear magnetic alignment within bcc FeRu. The noncollinear alignment is attributed to the competition between ferromagnetic and antiferromagnetic coupling in the film: ferromagnetic coupling between neighboring Fe atoms and antiferromagnetic coupling between Fe atoms separated by Ru atoms. On the other hand, hcp FeRu was found to be paramagnetic at room temperature and when cooled to 9.9 K.

Thin-film FeRu was recently shown to mediate a large noncollinear interlayer coupling between two hcp ferromagnetic layers for Ru concentrations from 20 to 38 at. % [18]. Here we show that, for the FeRu composition range of interest for noncollinear coupling, FeRu maintains hcp crystal structure. This is important for the epitaxial growth of these noncollinearly coupled trilayer structures.

Magnetic multilayer structures used for applications, including magnetic sensors and magnetic solid state memory, make extensive use of both Fe and Ru layers. Here we showed that the presence of a small amount of Ru in Fe can induce noncollinear magnetic alignment between Fe atoms, which can strongly affect the performance of these devices.

[1] P. A. Frey and G. H. Reed, The ubiquity of iron, ACS Chem. Biol. **7**, 1477 (2012).

[2] T. Takahashi and W. A. Bassett, High-pressure polymorph of iron, Science **145**, 483 (1964).

[3] O. Mathon, F. Baudelet, J. P. Itié, A. Polian, M. d'Astuto, J. C. Chervin, and S. Pascarelli, Dynamics of the magnetic and structural $\alpha-\epsilon$ phase transition in iron, Phys. Rev. Lett. **93**, 255503 (2004).

[4] A. B. Papandrew, M. S. Lucas, R. Stevens, I. Halevy, B. Fultz, M. Y. Hu, P. Chow, R. E. Cohen, and M. Somayazulu, Absence of magnetism in hcp iron-nickel at 11 K, Phys. Rev. Lett. **97**, 087202 (2006).

[5] S. Nasu, T. Sasaki, T. Kawakami, T. Tsutsui, and S. Endo, Mössbauer study of ϵ-Fe under an external magnetic field, J. Phys.: Condens. Matter **14**, 11167 (2002).

[6] B. W. Lebert, T. Gorni, M. Casula, S. Klotz, F. Baudelet, J. M. Ablett, T. C. Hansen, A. Juhin, A. Polian, P. Munsch, G. Le Marchand, Z. Zhang, J.-P. Rueff, and M. d'Astuto, Epsilon iron as a spin-smectic state, Proc. Natl. Acad. Sci. **116**, 20280 (2019).

[7] A. Monza, A. Meffre, F. Baudelet, J.-P. Rueff, M. d'Astuto, P. Munsch, S. Huotari, S. Lachaize, B. Chaudret, and A. Shukla, Iron under pressure: "Kohn tweezers" and remnant magnetism, Phys. Rev. Lett. **106**, 247201 (2011).

[8] W. J. Gallagher and S. S. P. Parkin, Development of the magnetic tunnel junction MRAM at IBM: From first junctions to a 16-Mb MRAM demonstrator chip, IBM J. Res. Dev. **50**, 5 (2006).

[9] J. Chen, Y. Lau, J. M. D. Coey, M. Li, and J. Wang, High performance MgO-barrier magnetic tunnel junctions for flexible and wearable spintronic applications, Sci. Rep. **7**, 42001 (2017).

[10] A. Guedes, M. Mendes, P. Freitas, and J. Martins, Study of synthetic ferrimagnet-synthetic antiferromagnet structures for magnetic sensor application, J. Appl. Phys. **99**, 08B703 (2006).

[11] L. J. Swartzendruber and B. Sundman, The Fe-Ru (iron-ruthenium) system, Bull. Alloy Phase Diagrams **4**, 155 (1983).

[12] W. E. Pöttker, C. Paduani, J. D. Ardisson, and M. I. Ioshida, Mössbauer effect studies of disordered Fe–Ru alloys, Phys. Status Solidi B **241**, 2586 (2004).

[13] A. Błachowski, K. Ruebenbauer, and J. Żukrowski, Spin- and charge-density waves around Ru impurities in $\alpha-$Fe alloys studied by ^{57}Fe Mössbauer spectroscopy, Phys. Rev. B **73**, 104423 (2006).

[14] H. Ohno, Antiferromagnetism in hcp iron-ruthenium and hcp iron-osmium alloys, J. Phys. Soc. Jpn. **31**, 92 (1971).

[15] D. I. C. Pearson and J. M. Williams, ^{57}Fe Mossbauer study of hexagonal phase iron alloys, J. Phys. F **9**, 1797 (1979).

[16] C. Petrillo, P. Postorino, A. Orecchini, and F. Sacchetti, Search for the elusive magnetic state of hexagonal iron: The antiferromagnetic $Fe_{71}Ru_{29}$ hcp alloy, J. Magn. Magn. Mater. **449**, 552 (2018).

[17] P. M. Marcus, V. L. Moruzzi, and S. L. Qiu, Type-II antiferromagnetism in compounds of iron with $4d$ metals, Phys. Rev. B **54**, 11933 (1996).

[18] Z. R. Nunn, C. Abert, D. Suess, and E. Girt, Control of the noncollinear interlayer exchange coupling, Sci. Adv. **6**, eabd8861 (2020).

[19] E. E. Fullerton and J. R. Childress, Spintronics, magnetoresistive heads, and the emergence of the digital world, Proc. IEEE **104**, 1787 (2016).

[20] R. Sbiaa, Magnetization switching by spin-torque effect in off-aligned structure with perpendicular anisotropy, J. Phys. D: Appl. Phys. **46**, 395001 (2013).

[21] R. Matsumoto, H. Arai, S. Yuasa, and H. Imamura, Spin-transfer-torque switching in a spin-valve nanopillar with a conically magnetized free layer, Appl. Phys. Express **8**, 063007 (2015).

[22] Y. Zhou, C. L. Zha, S. Bonetti, J. Persson, and J. Åkerman, Spin-torque oscillator with tilted fixed layer magnetization, Appl. Phys. Lett. **92**, 262508 (2008).

[23] See Supplemental Material at https://link.aps.org/supplemental/10.1103/PhysRevB.110.104429 for Supplemental Material I–VII.

[24] E. Raub and W. Plate, Die Eisen-Ruthenium Legierungen, Z. Metallkd. **51**, 477 (1960).

[25] P. Zaumseil, High-resolution characterization of the forbidden Si 200 and Si 222 reflections, J. Appl. Crystallogr. **48**, 528 (2015).

[26] S. Qadri, T. Keller, M. Laskoski, C. Little, P. Lubitz, M. Osofsky, and H. Khan, Structural and magnetic properties of nano-crystalline RuFe alloys prepared by organometallic synthesis, Appl. Phys. A **86**, 391 (2007).

[27] S. Qadri, T. Keller, M. Laskoski, E. Skelton, A. Husz, and N. Mahadik, Thermal expansion of RuFe alloys and its relationship to the high pressure phase of Fe, Appl. Phys. Lett. **94**, 171907 (2009).

[28] J. Chatterjee, R. C. Sousa, N. Perrissin, S. Auffret, C. Ducruet, and B. Dieny, Enhanced annealing stability and perpendic-ular magnetic anisotropy in perpendicular magnetic tunnel junctions using W layer, Appl. Phys. Lett. **110**, 202401 (2017).

[29] K. Yakushiji, A. Fukushima, H. Kubota, M. Konoto, and S. Yuasa, Ultralow-voltage spin-transfer switching in perpendicularly magnetized magnetic tunnel junctions with synthetic antiferromagnetic reference layer, Appl. Phys. Express **6**, 113006 (2013).

[30] B. Huang, H. Kobayashi, T. Yamamoto, T. Toriyama, S. Matsumura, Y. Nishida, K. Sato, K. Nagaoka, M. Haneda, W. Xie, Y. Nanba, M. Koyama, F. Wang, S. Kawaguchi, Y. Kubota, and H. Kitagawa, A CO adsorption site change induced by copper substitution in a ruthenium catalyst for enhanced CO oxidation activity, Angew. Chem., Int. Ed. **58**, 2230 (2019).

[31] C. E. Violet and D. N. Pipkorn, Mössbauer line positions and hyperfine interactions in α-iron, J. Appl. Phys. **42**, 4339 (1971).

[32] J. M. D. Coey, *Magnetism and Magnetic Materials* (Cambridge University Press, Cambridge, UK, 2010).

[33] C. Abert, S. Koraltan, F. Bruckner, F. Slanovc, J. Lisik, P. Omelchenko, E. Girt, and D. Suess, Origin of noncollinear magnetization coupling across RuX layers, Phys. Rev. B **106**, 054401 (2022).

[34] Z. R. Nunn, J. Lisik, P. Omelchenko, S. Koraltan, C. Abert, D. Suess, and E. Girt, Controlling the angle between magnetic moments of Co layers in Co|RuCo|Co, J. Appl. Phys. **133**, 123901 (2023).